Paleoclimate evidence of vulnerable permafrost during times of low sea ice

Vaks, A.*, Mason, A. J., Breitenbach, S. F. M., Kononov, A. M., Osinzev, A. V., Rosensaft, M., Borshevsky, A., Gutareva, O. S., and Henderson, G. M.

Climate change in the Arctic is occurring rapidly, and projections suggest the complete loss of summer sea-ice by the middle of this century[1]. The sensitivity of permanently frozen ground (permafrost) in the Northern Hemisphere to warming is less clear, and long-term trends are harder to monitor than those of sea-ice. Here we use paleoclimate data to indicate that Siberian permafrost is robust to warming when Arctic sea-ice is present, but vulnerable when it is absent. U-Pb chronology of carbonate deposits (speleothems) in a Siberian cave located at the southern edge of continuous permafrost, reveal periods when the overlying ground was not permanently frozen. The speleothem record starts 1.5 million years ago (Ma), a time when greater equator-to-pole heat transport led to a warmer northern hemisphere[2]. Speleothems' growth demonstrate that permafrost at the cave site was absent at this time, becoming more common from ≈1.35 Ma as the Northern Hemisphere cooled, and permanent after ≈0.4 Ma. This history mirrors that of year-round sea-ice in the Arctic Ocean, which was largely absent prior to ≈0.4 Ma[3], but continuous since that date. The robustness of permafrost when sea-ice is present, and increased permafrost vulnerability when sea-ice is absent can be explained by changes in both heat and moisture transport. Reduced sea-ice may contribute to warming of Arctic air[4-6] that can lead to warming far inland[7]. Open Arctic waters also increase the source of moisture and increase autumn snowfall over Siberia, insulating the ground from cold winter temperatures[8-10]. These processes explain the relationship between an ice-free Arctic and permafrost thawing prior to 0.4 Ma. If these processes continue during modern climate change, future loss of summertime Arctic sea-ice will enhance thawing of Siberian permafrost.

Arctic Ocean sea-ice declined increasingly rapidly in recent decades, with progressive ice thinning and increasing areas of open water during the summer-time[11]. Complete loss of summer sea-ice is expected by

the mid-21st century[1]. The recent loss of Arctic sea-ice raises concerns about its effects on other aspects of the global climate system, including potential acceleration of permafrost thawing[7]. Permafrost degradation as a result of anthropogenic global warming could amplify the climate change by releasing large volumes of carbon stored in permafrost in the form of CO_2 and methane[12]. In addition, permafrost thawing increases thermokarst development, coastal erosion, and liquefaction of ground previously cemented by ground ice, endangering infrastructures relying on permafrost as solid ground[13]. Establishing the relationship between loss of Arctic sea-ice and permafrost response is therefore an important goal.

Understanding of the response of permafrost to changing climate can be improved with knowledge of past environmental conditions. Precisely dated growth periods of speleothems (stalagmites, stalactites and flowstones) from caves located in permafrost regions have proved an effective tool for reconstruction of past permafrost extent and continuity[14]. Speleothems grow only when meteoric waters seep through the vadose zone into caves. When temperature in the upper vadose zone falls below 0°C throughout the year, water freezes, infiltration stops, and speleothem growth ceases. Speleothems found in modern permafrost regions are thus relicts from warmer periods when permafrost was absent, or when permafrost thawed temporarily[14,15]. Dating of these relicts allow comparison of periods of permafrost absence to other aspects of past environment.

In this study we reconstruct permafrost dynamics in central Eastern Siberia over the last 1,500 ka, using U-Pb dated speleothems from Ledyanaya Lenskaya Cave (60°22'15.60"N-116°56'47.30"E) (Fig. 1) located in the zone of present-day continuous permafrost (i.e., year-round frozen ground across the whole region[16], Extended Data (ED) 3). The study area is characterized by cold continental climate (Dfc according to the Köppen classification[17]), with mean July and January air temperatures of +18°C and -32°C respectively, and a mean annual air temperature (MAAT) of ~-6°C (ED 2), while annual precipitation is ~400 mm. The record from Ledyanaya Lenskaya Cave is compared with data from Botovskaya Cave (55°17'59.03"N-105°19'46.02"E) (Fig. 1), located in an area of discontinuous permafrost and MAAT of ~-2C (ED 2, 3).

This study continues the research of Vaks et al (2013)[14] which found that, in Ledyanaya Lenskaya Cave, the most recent permafrost thaw occurred at 429±23 ka[i] [18], during the warmth of Marine Isotopic Stage (MIS) 11[19]. That study was limited, however, by the ~500 ka range of U-Th chronology, meaning that older samples could not be analyzed. U-Pb chronology enables dating of such older speleothems. Here we use 52 U-Pb ages on 11 speleothems from Ledyanaya Lenskaya Cave to greatly extend the age range of known Siberian permafrost history. A smaller number of ages were also determined on three samples from the more southerly and warmer Botovskaya Cave[14] (Fig. 1) (see Methods, ED, and Data Tables 1 and 2 – for chronological methods and full results). Ages indicate a division of speleothem deposition in Ledyanaya Lenskaya Cave, and therefore of permafrost presence, into three distinct periods (Figs. 2A, 3A):

During the period from ***1,500 to ~1,350 ka*** speleothems apparently grew continuously (within the limits of analytical uncertainties), suggesting discontinuous or absent permafrost above the cave. Globally, this interval spans MIS-50 to MIS-43 and is characterized by glacial-interglacial cycles with 41 ky periodicity[19]. Most of the analyzed speleothems in Ledyanaya Lenskaya Cave grew in this period (7 out of 11) (ED 4). These oldest vadose speleothems were the first deposited directly on the cave host-rock, heralding the onset of vadose conditions at this site, and suggesting that, before 1,500 ka, the cave may have been located below the local groundwater level. The current groundwater table is located ~50 m below the cave's entrance and controlled by the nearby Lena River.

The period from ***~1,350 to ~400 ka*** is defined by intermittent speleothem growth with long-lasting hiatuses without speleothem deposition. These growth cessations are likely to indicate continuous periods of permafrost and are found at the time of most glacial MISs and some interglacial MISs. Speleothem growth, demonstrating the absence of permafrost, occurred during most interglacials (Fig. 2A). Since ~1,300 ka speleothems only grew in the shallower portion of the cave (15-20 m below the surface) and not in the deeper area (~60 m) (Fig. 2A, 3A; ED 1). This may indicate that the permafrost was thawing only to depth

[i] The original age sited by Vaks et al (2013) is 427±23 ka, the age above is re-calculated using updated half-lives of ^{234}U and ^{230}Th[18]

of 15-20 m, whereas relict permafrost remained at greater depth, showing that the duration of thawing periods was relatively short and/or that MAAT were reduced compared to the period prior to 1,300 ka.

From ~400 ka until present speleothem growth ceased completely and permafrost appears to have been continuous above Ledyanaya Lenskaya Cave (Fig. 2A, 3A and ED)[14].

Caves located further south near Lake Baikal (Botovskaya and Okhotnichya) (Fig. 1) show speleothem deposition during warm periods during the last 700 ka (this study, and Vaks et al (2013)[14] (Fig. 2A and ED)). These southerly caves indicate that climate in southern Siberia was warmer than in Ledyanaya Lenskaya Cave, enabling deposition of speleothems, while in Ledyanaya Lenskaya Cave to the north speleothem growth ceased completely for the entire last ~400 ka.

Based on data for the last 500 ka, Vaks et al (2013)[14] found permafrost thawing at Ledyanaya Lenskaya Cave during the unusual warmth of MIS-11 (429±23 ka) but not in younger interglacials. They suggested that an increase in global mean surface temperature of 1.5°C (above preindustrial levels) represents the threshold above which continuous permafrost thaws at its southern fringes. Our new results indicate that substantial speleothem deposition occurred prior to MIS-11, when global mean surface temperatures (as indicated by Pacific Warm Pool sea-surface-temperatures) were lower than those of MIS-11 (e.g. MIS 25, 19, 15), and even lower than today (e.g. MIS 23, Fig. 2C)[20]. These earlier periods of speleothem growth indicate that global mean surface temperature is not the only control on the extent of Siberian permafrost. Other possible controls may include: 1) local summer insolation; 2) paleo-geographic changes; 3) greater poleward heat transport in the Northern hemisphere, leading to relatively warmer conditions in the North Atlantic, Arctic, and/or over the Eurasian landmass; or 4) Arctic Ocean sea-surface temperatures (SST) and the extent of Arctic summer sea-ice cover.

The intensity of summer insolation on latitude 60ºN (Fig. 2D)[21] may directly affect Siberian summer temperatures and therefore influence permafrost thawing. Many periods of speleothem deposition occurred when July insolation was high (i.e. >500 W/m^2), but there is no direct relationship between insolation and

96 thawing of permafrost. No thawing took place during periods of insolation >500 w/m^2 during the last 400
97 ka, but thawing did occur at much lower insolation earlier in the record. Local summer insolation is
98 therefore not the key factor determining the presence of permafrost above Ledyanaya Lenskaya Cave.

99 Arctic paleogeographic conditions during *interglacials* of the entire last 1,500 ka were similar to present,
100 with the open Bering Strait, enabling water exchange between Pacific and Arctic oceans[22]. The Atlantic
101 Meridional Overturning Circulation (AMOC) transports heat from the tropics to the northern Atlantic
102 Ocean thereby increasing the heat flux to high latitudes in continental Eurasia and the Arctic[23]. The period
103 between ~2.4 and 1.3 Ma was characterized by enhanced AMOC, causing heat piracy from the southern to
104 the northern hemisphere, which was consequently relatively warm[2]. This enhanced northward heat flux
105 caused significantly warmer SSTs in the North Atlantic than those of most of Middle-Late Quaternary and
106 Holocene[2] (Fig. 3C, D). After ~1,300 ka the AMOC gradually weakened, leading to concurrent lowering
107 of North Atlantic SST of 1.5°C to 3°C [24] (Fig. 3C, D). This is likely to cause progressive cooling of the
108 Eurasian landmass on long-term scale and could influence the presence of permafrost (which is much less
109 common early in the record when the northern hemisphere was warmer on average). Again, there is no
110 simple relationship between speleothem growth in Ledyanaya Lenskaya Cave and North Atlantic warmth:
111 periods of significant North Atlantic warmth during the last 400 ka are not associated with permafrost
112 thawing. For example: MIS-9 (Fig. 3C, D) and MIS-5 (Fig. 3D) were warmer than all other times in the
113 last ~1,300 ka, but there is no permafrost thawing above Ledyanaya Lenskaya Cave. Of these, MIS-5 is
114 particularly notable because both the Pacific Warm Pool (Fig. 2C) and North Atlantic (Fig. 3D) were
115 warmer than many earlier thaw periods, and as warm as interglacials in the period of 1,500-1,300 ka when
116 the permafrost above the Ledyanaya Lenskaya Cave was discontinuous or absent. Yet, there is no evidence
117 for permafrost thawing above Ledyanaya Lenskaya Cave at MIS-5 (Fig. 3A).

118 It is striking that the permanent presence of permafrost since 400 ka initiates at the same time as perennial
119 sea-ice is established in the Arctic Ocean (Fig. 3A, 3E). The appearance of perennial sea-ice is marked by
120 an abrupt increase in the appearance of sea-ice-associated fauna in the western Arctic Ocean[3] (Fig.3E) and

121 the disappearance from the Arctic Ocean of fauna that today is found in the North Atlantic[25]. The perennial
122 Arctic sea-ice (Fig. 3E) remained intact even during MIS-9 and MIS-5e, when both the tropics (Fig. 2C)
123 and North Atlantic (Fig. 3C, D) were particularly warm.

124 Climatic models for present and past climates indicate a relationship between Arctic sea-ice and Eurasian
125 permafrost caused by changes in atmospheric heat transport[5,26]. Removal of Arctic sea-ice warms the air
126 above the sea surface[5], increasing the moisture content of the atmosphere, and therefore increasing the
127 transport of both sensible and latent heat from the ocean via atmospheric transport to continental interiors[4].
128 Resulting warming can penetrate up to 1,500 km inland, peaking in autumn, and leading to permafrost
129 degradation[7]. An open Arctic Ocean also leads directly to increased transport of moisture from the sea to
130 the continent. High d-excess values of autumn atmospheric precipitation in Siberia show that open Arctic
131 Ocean comprises a substantial moisture source that is shut down when the Arctic ice cover is established
132 in early winter[27]. Models show that future increase in Arctic precipitation will come mainly from
133 evaporation from Arctic Ocean due to retreating sea-ice, and not from enhanced moisture transport from
134 lower latitudes[28]. At present, decreased sea-ice cover in the autumn increases moisture and leads to heavier
135 autumn snowfall over Siberia[8,9]. Thicker autumn snow cover insulates the ground from cold winter
136 temperatures, increasing winter and mean annual ground temperatures[9,10]. This effect, well known to
137 influence seasonal vegetation[10], has not previously been recognized as a significant long-term control on
138 the extent of permafrost, but the strong relationship between perennial sea-ice and permafrost observed in
139 this study suggests it may be an important controlling factor. The appearance of perennial sea-ice 400 ka
140 ago decreases the Arctic heat (sensible and latent) and moisture source[27] cooling the Arctic air and reducing
141 snowfall on the continent. That may lead to poorer ground insulation and lowering of ground temperature,
142 assisting to the establishment of continuous permafrost[29]. Future loss of summer sea-ice may have the
143 opposite effect, warming ground temperatures and speeding the thawing of permafrost.

144 The stability of continuous permafrost near its modern southern boundary in Siberia hinges on perennial
145 sea-ice cover in the Arctic Ocean. Although the speleothems' record of this study also indicates intervals

of permafrost prior to the formation of perennial sea-ice on ~400 ka, such permafrost was prone to thawing in times of higher Northern Atlantic and/or global mean temperature. The long-term cooling of Arctic Ocean that occurred between ~1,350 ka and ~400 ka eventually reached a temperature threshold for the formation of perennial Arctic sea-ice, which stabilized the presence of continuous permafrost in Siberian regions where it remains today. This new record indicates that, under future open-water Arctic scenarios as predicted for later this century[30], this stabilization is likely to be removed, enhancing the northerly retreat of continuous permafrost.

Acknowledgments

We would like to thank Kazanzev, I. G., Stol'arov, V. A., Sokol'nikov, D. S., and other Speleoclub Arabica members for their help with expeditions' organizations, mapping the caves and collecting samples. We would like to thank Alexeev, S. V, Kozireva, E. A., Pellinen, V, A., and Svetlakov, A. A., from Institute of Earth's Crust of the Russian Academy of Sciences (IEC RAS) in Irkutsk for help in the field and with samples shipment. We thank Balaev, V. A. and Alexioglo, V. V., from Lensk, for their help during the fieldwork in Ledyanaya Lenskaya Cave. We thank Kwiecien, O. from Ruhr University Bochum, Germany, Lechleitner, F. from University of Oxford, UK, and Brall, N. from University of Lyon, France, for help with samples collecting in Botovskaya Cave, We thank Cohen, B. from Geological Survey of Israel for the help with graphic work. We thank Schirrmeister, L., Parrish, R., and third anonymous reviewer for useful comments that helped to substantially improve the quality of this paper. We also gratefully acknowledge the NOAA Air Resources Laboratory (ARL) for the provision of the HYSPLIT transport and dispersion model and/or READY website (https://www.ready.noaa.gov) used in this publication. This work was funded by NERC Fellowship NE/G013829/1, NERC Standard Grant NE/K005057/1, Royal Society grant JP080831 and RFBR joint grant 09-05-92605 KO_a.

Author contributions:

A.V., G.M.H. and S.F.M.B. devised the approach of using caves to reconstruct permafrost, and raised the funding for this research. A.V., A.V.O., S.F.M.B., and O.S.G. conducted the field work, with help from A.M.K.. A.J.M. led the development and application of the chronological work, with input from A.V. and G.M.H.. A.V.O., M.R., A.B., S.F.M.B. and A.M.K. drew the maps (permafrost and caves) with input from all authors. A.V. led the interpretation of the data, and the writing of the manuscript, with input from all authors.

References:

1 IPCC, 2013: Climate Change 2013: The Physical Science Basis. Contribution of Working Group I to the Fifth Assessment Report of the Intergovernmental Panel on Climate Change. 1535 pp (Cambridge University Press, Cambridge, United Kingdom and New York, NY, USA, 2013).

2 Bell, D. B., Jung, S. J. A. & Kroon, D. The Plio-Pleistocene development of Atlantic deep-water circulation and its influence on climate trends. *Quaternary Science Reviews* **123**, 265-282, doi:http://dx.doi.org/10.1016/j.quascirev.2015.06.026 (2015).

3 Cronin, T. M. *et al.* Enhanced Arctic Amplification Began at the Mid-Brunhes Event ~400,000 years ago. *Scientific Reports* **7**, 14475, doi:10.1038/s41598-017-13821-2 (2017).

4 Ballantyne, A. P. *et al.* The amplification of Arctic terrestrial surface temperatures by reduced sea-ice extent during the Pliocene. *Palaeogeography, Palaeoclimatology, Palaeoecology* **386**, 59-67, doi:https://doi.org/10.1016/j.palaeo.2013.05.002 (2013).

5 Dai, A., Luo, D., Song, M. & Liu, J. Arctic amplification is caused by sea-ice loss under increasing CO2. *Nature Communications* **10**, 121, doi:10.1038/s41467-018-07954-9 (2019).

6 Screen, J. A. & Simmonds, I. The central role of diminishing sea ice in recent Arctic temperature amplification. *Nature* **464**, 1334, doi:10.1038/nature09051 https://www.nature.com/articles/nature09051#supplementary-information (2010).

7 Lawrence, D. M., Slater, A. G., Tomas, R. A., Holland, M. M. & Deser, C. Accelerated Arctic land warming and permafrost degradation during rapid sea ice loss. *Geophysical Reasearch Letters* **35**, 1-6 (2008).

8 Liu, J., Curry, J. A., Wang, H., Song, M. & Horton, R. M. Impact of declining Arctic sea ice on winter snowfall. *Proceedings of the National Academy of Sciences*, doi:10.1073/pnas.1114910109 (2012).

9 Park, H., Walsh, J. E., Kim, Y., Nakai, T. & Ohata, T. The role of declining Arctic sea ice in recent decreasing terrestrial Arctic snow depths. *Polar Science* **7**, 174-187, doi:https://doi.org/10.1016/j.polar.2012.10.002 (2013).

10 Zhang, T. Influence of the seasonal snow cover on the ground thermal regime: An overview. *Reviews of Geophysics* **43**, doi:doi:10.1029/2004RG000157 (2005).

11 Serreze, M. C. & Stroeve, J. Arctic sea ice trends, variability and implications for seasonal ice forecasting. *Philosophical Transactions of the Royal Society A: Mathematical, Physical and Engineering Sciences* **373**, doi:10.1098/rsta.2014.0159 (2015).

12 Schuur, E. A. G. *et al.* Vulnerability of Permafrost Carbon to Climate Change: Implications for the Global Carbon Cycle. *BioScience* **58**, 701-714, doi:10.1641/b580807 (2008).

13 Anisimov, O. & Reneva, S. Permafrost and Changing Climate: The Russian Perspective. *AMBIO: A Journal of the Human Environment* **35**, 169-175, doi:10.1579/0044-7447(2006)35[169:pacctr]2.0.co;2 (2006).
14 Vaks, A. *et al.* Speleothems Reveal 500,000-Year History of Siberian Permafrost. *Science* **340** 183-186, doi:10.1126/science.1228729 (2013).
15 Lauriol, B., Ford, D. C., Cinq-Mars, J. & Morris, W. A. The chronology of speleothem deposition in northern Yukon and its relationships to permafrost. *Canadian Journal of Earth Sciences* **34**, 902-911, doi:di:10.1139/e17-075 (1997).
16 Brown, J., Ferrians, J. O. J., Heginbottom, J. A. & Melnikov, E. S. in *Circum-Arctic map of permafrost and ground-ice conditions, in Circum-Pacific Map Series CP-45, scale 1:10,000,000* (US Geological Survey in Cooperation with the Circum-Pacific Council for Energy and Mineral Resources., Washington, DC: U.S., 1997).
17 Peel, M. C., Finlayson, B. L. & Mcmahon, T. A. Updated world map of the Köppen-Geiger climate classification. *Hydrology and Earth System Sciences Discussions, European Geosciences Union* **11**, 1633-1644 (2007).
18 Cheng, H. *et al.* Improvements in 230Th dating, 230Th and 234U half-life values, and U–Th isotopic measurements by multi-collector inductively coupled plasma mass spectrometry. *Earth and Planetary Science Letters* **371-372**, 82-91, doi:https://doi.org/10.1016/j.epsl.2013.04.006 (2013).
19 Lisiecki, L. E. & Raymo, M. E. A Pliocene-Pleistocene stack of 57 globally distributed benthic $\delta^{18}O$ records *Paleoceanography* **20**, doi:10.1029/2004PA001071 (2005).
20 Hansen, J. *et al.* Global temperature change. *Proceedings of the National Academy of Sciences* **103**, 14288-14293, doi:10.1073/pnas.0606291103 (2006).
21 Laskar, J. *et al.* A long-term numerical solution for the insolation quantities of the Earth. *Astronomy and Astrophysics* **428**, 261-285, doi: 10.1051/0004-6361:20041335 (2004).
22 Kender, S. *et al.* Closure of the Bering Strait caused Mid-Pleistocene Transition cooling. *Nature Communications* **9**, 5386, doi:10.1038/s41467-018-07828-0 (2018).
23 Maroon, E. A., Kay, J. E. & Karnauskas, K. B. Influence of the Atlantic Meridional Overturning Circulation on the Northern Hemisphere Surface Temperature Response to Radiative Forcing. *Journal of Climate* **31**, 9207-9224, doi:10.1175/jcli-d-17-0900.1 (2018).
24 Lawrence, K. T., Sosdian, S., White, H. E. & Rosenthal, Y. North Atlantic climate evolution through the Plio-Pleistocene climate transitions. *Earth and Planetary Science Letters* **300**, 329-342, doi:http://dx.doi.org/10.1016/j.epsl.2010.10.013 (2010).
25 Cronin, T. M. *et al.* Quaternary ostracode and foraminiferal biostratigraphy and paleoceanography in the western Arctic Ocean. *Marine Micropaleontology* **111**, 118-133, doi:https://doi.org/10.1016/j.marmicro.2014.05.001 (2014).
26 Vandenberghe, J. *et al.* Eurasian permafrost instability constrained by reduced sea-ice cover. *Quaternary Science Reviews* **34**, 16-23, doi:https://doi.org/10.1016/j.quascirev.2011.12.001 (2012).
27 Kurita, N. Origin of Arctic water vapor during the ice-growth season. *Geophysical Research Letters* **38**, doi:10.1029/2010gl046064 (2011).
28 Bintanja, R. & Selten, F. M. Future increases in Arctic precipitation linked to local evaporation and sea-ice retreat. *Nature* **509**, 479, doi:10.1038/nature13259 (2014).
29 O'Neill, H. B. & Burn, C. R. Impacts of variations in snow cover on permafrost stability, including simulated snow management, Dempster Highway, Peel Plateau, Northwest Territories. *Arctic Science* **3**, 150-178, doi:10.1139/as-2016-0036 (2017).

30 Barnhart, K. R., Miller, C. R., Overeem, I. & Kay, J. E. Mapping the future expansion of Arctic open water. *Nature Climate Change* **6**, 280, doi:10.1038/nclimate2848 https://www.nature.com/articles/nclimate2848#supplementary-information (2015).

Figure captions:

Figure 1: Study area and permafrost maps. (A) Permafrost map of northern Eurasia with the research area marked by the black rectangle, continuous permafrost in purple, discontinuous permafrost in green, and the area with no permafrost in yellow; (B) Extent of permafrost types in eastern Siberia[16] and the location of Ledyanaya Lenskaya, Botovskaya and Okhotnichya caves, marked by black stars. Cities and towns are marked by grey circles. Permafrost types (see legend) are defined by the percentage of the year-round frozen ground.

Figure 2: Siberian speleothem deposition periods compared to records of MIS, Pacific warm pool SSTs and July mean insolation on 60˚N. (A) Distribution of speleothem U-Pb and U-Th ages (±2σ) in Ledyanaya Lenskaya Cave (purple circles) and in Botovskaya Cave (light blue circles at) in time (ka) and space (latitude ˚N). Ages of Ledyanaya Lenskaya SLL14 speleothems (60 m below the surface) are marked by dark purple circles, and of SLL9/SLL10 speleothems (15-20 m below the surface) by light purple circles. Purple vertical rectangles show how periods of speleothem growth in Ledyanaya Lenskaya Cave relate to other climatic records. (B) Benthic $\delta^{18}O$ stack[19] with glacial MIS numbers below and interglacial above; (C) Pacific Warm Pool Mg/Ca inferred SST changes during the last 1400 ka, which are considered to be a reasonable reflection of changes in mean Earth surface temperature[20]. The preindustrial SST is marked by lower dotted red horizontal line and abbreviation "PI-SST". The SST 1.5˚C higher than preindustrial level is marked by upper dotted red line and abbreviation "+1.5˚C-SST"; (D) July mean insolation at 60°N[21].

Figure 3: Siberian speleothem deposition periods compared to records of MIS, North Atlanic SST and presence of sea-ice in Arctic Ocean. (A) Distribution of speleothem U-Pb and U-Th ages (±2σ) in

time and space (details in caption of Fig. 2). (B) Benthic $\delta^{18}O$ stack[19] with glacial MIS numbers below and interglacial above; (C) North Atlantic mid-latitude (41°N, 33°W) $U^{k'}_{37}$ SST as recorded in ODP-607 core[24], and with a 81 data point (~200 ka) running average showing a ≈3°C decrease in the long-term SST; (D) North Atlantic high-latitude (58°N, 16°W) $U^{k'}_{37}$ SST as recorded in ODP-982 core[24], and with 81 data point (~200 ka) running average showing ≈1.5°C decrease in the long-term SST; (E) Percent abundance of genus *Polycope*, a benthic opportunistic genus signifying high local surface productivity in Arctic sea-ice margin environments, and therefore presence of the sea-ice in Northwind Ridge, western Arctic Ocean[3].

Methods

Description of the caves:

Ledyanaya Lenskaya Cave:

The cave is located 116 km E-S-E of the town of Lensk, 180 m above sea level, with the cave entrance located on the north-eastern riverbank in a cliff ~50 m above the Lena River. The local vegetation is sub-boreal taiga forest[31]. The cave is developed in Ediacaran limestones and marls and its length is mapped to ~216 m. A ~90 m long main passage is ascends by ca. 15° in a N-NE direction, ending in a central ~55 m long and 10-20 m wide hall, with ceiling height up to 8 m. The hall is mostly filled with massive ice several meters thick. A narrow passage leads from its top to the cave's upper section. The latter is ~70 m long ascending by ~20°, and consists of two chambers connected by a narrow passage and partly filled by ice. The walls of these chambers are partly covered by flowstone and stalactites (SLL14, taken in 2014, ED 1A). Ca. 50 m from the main entrance a narrow slightly ascending ~40 m long corridor splits from the main passage in E-NE direction, and ends in small chambers in which vadose speleothems were collected (SLL9 and SLL10, taken in 2009-2010, ED 1A). The depth of this chamber below the surface is 15-20 m, and the depth of the large hall is ~60 m.

The cave air temperature was monitored using HOBO UA Pendant Temperature Loggers from March 2010 to May 2013 (Logger "Siberia 7") and November 2013 (Logger "Siberia 6") (ED 2A, B). The loggers' measurement uncertainty is ±0.47°C. The temperature in the central hall with massive ice was measured with logger "Siberia 6" (ED 1A) and was found to vary between -0.1°C and 0.0°C in early spring, and between +0.6°C and +0.7°C in summer (ED 2A). Logger "Siberia 7" measured the temperature in the chamber with speleothems SLL9 and SLL10, and the temperature there is relatively stable at ~+0.3°C (ED 2A). Although in both places temperatures are slightly above zero, no water seepage or speleothem growth was found beyond several meters from the entrance, showing that the rock above the cave is frozen year-round. In the uppermost cave chambers where SLL14 speleothem samples were collected, the temperature in January 2014 was 0°C and the ice was dry. According to Lensk meteorological station (ED 2B) the mean annual air temperature (MAAT) between 2010 and 2013 was ~ -6°C, thus the cave is by 6°C warmer. The cave's ascending morphology with the entrance being its topographically lowest point, causes warm humid air being trapped inside during the summer months. Formation of ice in the uppermost parts of the cave shows that the cooling that creates the ice occurs when warm and moist air comes in contact with the sub-zero temperature of the cave walls[32]. This is also supported by the permafrost map, that shows continuous permafrost (type 18) above the Ledyanaya Lenskaya Cave[33] (ED 3A). More information about the cave can be found in Supplementary Online Materials of Vaks et al (2013)[14].

Botovskaya Cave:

The cave system is located 58 km N-NE of the town of Zhigalovo, 750 m above sea level, at the head of a small valley NE of the Boti River, that joins the Lena River 8.6 km SE of the cave. The vegetation is sub-boreal taiga forest[31]. The cave is located in Ordovician limestones and sandstones, and is the longest cave system in Russia, reaching a total length of >69 km and depth of up to 130 m below the surface, comprising a horizontal maze of thousands of passages developed along the crisscross system of tectonic fissures (ED 1B).

Cave air temperatures were monitored using HOBO UA Pendant Temp loggers from February 2010 to February 2016. The temperatures in the deeper parts of the cave are stable at +1.9±0.3°C in its but vary from -0.2°C to +1.6°C near the entrance, with minima in winter and maxima in the summer (ED 2C). Surface air temperatures (SAT) outside the cave were also monitored by a HOBO logger tied on the northern shady side of a big tree 2 m from the ground. Mean annual SAT is -2.1°C, varying between summer and winter extremes from +37°C to <-40°C (-40°C is the minimum limit of the logger; during two nights in winter 2010-11 the minimum temperature dropped below -40°C). MAAT is thus lower than the cave air temperature by 3-4°C (ED 2D).

Regional permafrost is discontinuous and found below the Boti River valley and its slopes, but is absent from the plateau above the inner parts of Botovskaya Cave[33] (ED 3B). The eastern part of the cave ("New World") is where the most water seepage and modern speleothem deposition occurs today (ED 3B). This cave section is located below a small surface depression that hosts an intermittent stream that allows rain/snowmelt water to seep into the cave. Thermal energy from infiltrating water probably contributes to an absence of permafrost in this area. Speleothem samples were collected in the "New World" section of the cave. The western part of the cave ("Old World") is drier, with some passages near the entrance clogged with massive ice.

Speleothem petrography:

In Ledyanaya Lenskaya Cave the speleothem cover on the cave walls and floor is usually 5-10 cm thick. Speleothems consist of several calcite horizons, each composed of brown or grey columnar calcite crystals usually clean from detrital material (ED 4, 6A, B). These calcite horizons are separated by whitish or beige thin (<2 mm) layers of microcrystalline calcite, sometimes containing pieces of marl and limestone host rock. These layers represent growth hiatuses, sometimes with pieces of broken host rock from the cave ceiling remaining on the ancient speleothem surface.

In Botovskaya Cave speleothem deposition is much more widespread and massive than in Ledyanaya Lenskaya Cave. Here the thickness of the speleothems is many tens of cm, showing that compared to

Ledyanaya Lenskaya Cave the humid and warmer climate of the area provided speleothems with better opportunities to grow (ED 5). Active speleothems are also found in this cave. Unlike in Ledyanaya Lenskaya Cave, most speleothems in Botovskaya Cave are composed of aragonite (ED 6 C, D), but with some calcite speleothems (e.g. stalagmite SB-6919), and some speleothems comprising alternate aragonite and calcite layers (e.q. stalagmite SB-01112). Apparent growth breaks, sometimes separating calcite and aragonite layers, are common.

Methods used in the study

The speleothems were sectioned using a diamond saw. For the purpose of U-Th dating between 10 and 250 mg of powder was drilled from each sampled horizons using 0.8-1 mm drill bits. Speleothem mineralogy was examined at ETH Zurich, Switzerland, using a Bruker, AXS D8 Advance powder XRD diffractometer, equipped with a scintillation counter and an automatic sampler. Macro and microscope inspection shows that all horizons chosen for dating had a typical columnar petrography in calcite and fibrous petrography in aragonite (ED 6), with almost no voids or re-crystallization marks, suggesting that they likely maintained closed system conditions for U-series chronology (except for some growth hiatuses, such as that in SB-01112, ED 5).

U-Pb chronology

Analytical methodology

Ages were determined by isotope dilution using a mixed ^{236}U-^{204}Pb-^{230}Th spike[34] and a first generation Nu Plasma MC-ICP-MS. Subsamples were cut using a small diamond saw and transferred to acid-cleaned (1-2 M HNO_3 for >3 days) 15 ml polypropylene bottles. The subsamples were then sonicated repeatedly in 18 MΩ.cm water until no suspended fines were visible, rinsing between each wash. Subsamples were then twice acid cleaned in distilled 2 % HNO_3 with sonication to remove any residual dirt. Following each wash, samples were thoroughly washed with 18 MΩ.cm water and sonicated to remove any residual acid and dislodged surface material. Each acid wash was removed before the acid reaction completed, to prevent adsorption of dissolved ions back on to the surface of the sample.

One-two drops (~30 μL/drop) of spike were added directly to the acid cleaned carbonate and gently agitated to mix as the spike fully dissolved the sample. Once visible reaction was complete, the solution was diluted to ca. 15 ml with 18 MΩ.cm water, thoroughly shaken to homogenise, and then immediately analysed, with no pre-concentration of U and Pb.

Analyses followed a six-step routine. In steps 0, 1, 2, and 3, ^{208}Pb, ^{207}Pb, ^{206}Pb, $^{204}Pb+^{204}Hg$ and ^{202}Hg were measured using three ion-counters at two AMU spacing. The relative gains of the ion-counters were determined by stepping $^{204}Pb+^{204}Hg$ alternately in to each collector. ^{202}Hg was monitored to correct for ^{204}Hg on ^{204}Pb. In steps 4 and 5 ^{238}U was measured on a Faraday cup, with ^{235}U and ^{236}U measured alternately on both Faraday and ion counter; this allows using the Faraday/Faraday $^{238}U/^{235}U$ ratio, or the Faraday/ion counter $^{238}U/^{235}U$ ratio depending on ^{235}U signal intensity. Faraday/Faraday ratios were normally used for both the $^{238}U/^{235}U$ and the $^{238}U/^{236}U$.

Mass fractionation was estimated using the measured $^{238}U/^{235}U$ ratio of the samples and an assumed natural value 137.75[35]. Based on previous testing of the instrument, the mass fractionation for Pb was assumed to be 2‰/AMU higher than for U[36].

Prior to first analysis, the Nu Instruments DSN100 sample introduction system and sample lines were cleaned with 10% HNO_3, 2% HNO_3 and 18 MΩ.cm water. A dedicated set of B-type cones reserved for very low level Pb work were used. These were gently cleaned by rinsing with DI water prior to use to remove excessive Ca build-up from the skimmer orifice. As far as possible, the surface coating on the cones was not disturbed. The instrument was then initially tuned and optimised with a 100 ppt Tl solution and diluted natural U solution. Intentional addition of Pb was avoided during tuning to prevent re-contamination of the instrument, but sufficient Pb-blank is present in the Tl solution to see the Pb peaks on the ion counters. Peak shape and optimisation was then re-checked on samples; focusing settings for

404 the zoom optics often changed substantially from the nominally clean Tl solution to the matrix-heavy
405 samples, especially following cleaning of the cones. Gas flows were also re-optimised to suppress
406 interferences (probably from Sr_2O_2) which manifest as superimposed peaks ~0.2 AMU lighter than the Pb
407 peaks, especially on ^{208}Pb. Optimisation was checked again after an initial couple of sacrificial analyses
408 and regularly during the analytical session. The DSN100 was re-cleaned with 18 MΩ.cm water every 1-2
409 days to remove Ca build-up and U and Pb blank.
410
411 Separate sample aliquots up to c. 0.2 g were dissolved and purified to obtain U cuts for measurement of
412 the $^{234}U/^{238}U$ ratio. Purification used 2 ml columns with AG1X8 anion exchange resin. Samples were
413 loaded in, and Ca eluted with c. 10M HCl. U was eluted with 18 MΩ.cm water. The purified U was
414 measured on the same instrument, with the ^{234}U and ^{238}U measured on ion counter and Faraday collectors,
415 respectively. Standard bracketing with CRM145 (CRM112A) was used to correct both for mass
416 fractionation and ion counter gain.
417
418 Non-radiogenic Pb correction
419 Model ages were calculated from each pair of U-Pb and $^{234}U/^{238}U$ analyses. The ^{238}U-^{206}Pb decay
420 provides the age data used here, but the ^{235}U-^{207}Pb system was also measured and provides an assessment
421 of concordance, and thus confidence in obtained ages.
422
423 Ages were calculated using an estimated $^{208}Pb/^{206}Pb$ (and $^{208}Pb/^{207}Pb$) ratio for the initial non-radiogenic
424 Pb and, the modern-day measured disequilibrium in the $^{234}U/^{238}U$ ratio to constrain the initial $^{234}U/^{238}U$
425 ratio. ^{208}Pb is assumed to be entirely non-radiogenic on the basis that the ^{232}Th is typically at very low
426 concentration in speleothems and that samples are young compared to the ^{232}Th half-life. Common
427 $^{208}Pb/^{206}Pb$ (and $^{208}Pb/^{207}Pb$) for the non-radiogenic Pb correction was estimated by a combination of:

1) identifying and analysing unradiogenic parts of the sample, not greatly modified by Pb from decay.
2) retrospectively picking approximate isochrons from the data, on the basis that given a large number of analyses the following are likely: a) age overlap between samples/subsamples can be expected and hence some clumping of analyses along mixing lines between the initial Pb composition and the radiogenic composition for a given (approximate) age; b) data should fan around the initial Pb composition; c) subsamples of roughly the same age, can, to a first approximation be grouped based on the observed $^{234}U/^{238}U$ ratio. The latter is somewhat limited by initial $^{234}U/^{238}U$ variation, but surviving ^{234}U disequilibrium decreases by a factor of 2 for each ^{234}U half-life, so for a spread of ages over a few hundred ka or more, the variations due to decay of ^{234}Uxs will dominate over variations in the initial ratio.
3) Linear regressions[35,36] through groups of data of similar age in ^{234}U(or ^{238}U)/^{206}Pb – $^{208}Pb/^{206}Pb$ isotope space allow an estimate of the initial $^{208}Pb/^{206}Pb$ ratio ($^{235}U/^{207}Pb$ – $^{208}Pb/^{207}Pb$ isotope space for the initial $^{208}Pb/^{207}Pb$ ratio). Only groups containing relatively non-radiogenic analyses (ideally stratigraphically bracketed by more radiogenic analyses) were used, to minimise the effect of incorrectly grouping samples of different age. The groupings used and regression results are shown in Data Table 1 and illustrated in ED 7.

A common $^{208}Pb/^{206}Pb$ ratio of 1.471±0.100 (and $^{208}Pb/^{207}Pb$ ratio of 2.465±0.136) (95% confidence) was used for the Ledyanaya Lenskaya Cave samples (ED 7). The former value is based mainly on a single grouping of samples that include the least radiogenic Ledyanaya Lenskaya analysis, but is in agreement with a second generally more radiogenic grouping. All other Ledyanaya Lenskaya data (except data rejected in Data Table 1) are consistent with this common $^{208}Pb/^{206}Pb$ ratio (ED 7).

For Botovskaya Cave samples, which include highly non-radiogenic material, a common $^{208}Pb/^{206}Pb$ ratio of 1.997±0.213 (and $^{208}Pb/^{207}Pb$ ratio of 2.419±0.123) (95% confidence) was determined in a similar way.

Formatted: English (United States)
Formatted: English (United States)
Field Code Changed
Field Code Changed
Field Code Changed
Formatted: English (United States)
Formatted: English (United States)

As the Botovskaya data also includes some analyses that are almost entirely non-radiogenic, these have also been taken into account. Sample groupings and regression results are again shown in ED 7 and Data Table 1.

The rather different values of the common Pb composition between the two caves are likely attributable to host rock composition. Botovskaya and Ledyanaya Lenskaya caves are hosted in rocks of Ordovician and Late Proterozoic age, respectively, which have had long periods to evolve distinctive Pb compositions prior to the formation of the speleothems they now host.

The use of model ages involves some degree of assumption about the uniformity of the common Pb composition. Consequently, an indication of the sensitivity of a particular age to the common Pb correction is given in Data Table 1 and ED 7, and found to be small compared to quoted uncertainties.

Pb blanks have not been separately corrected for and are dealt with as part of the total correction for non-radiogenic Pb. Given that a number of analyses yielded >99% radiogenic ^{206}Pb, the Pb blank can be considered a generally minor source of non-radiogenic Pb. Sample ^{204}Pb was corrected in the isotope dilution calculation using ^{208}Pb as a proxy, assuming a natural $^{208}Pb/^{204}Pb$ ratio of 37.1±10 (95% confidence). For most analyses, >99% of the total ^{204}Pb originated from the tracer, so the correction is small.

Ages were calculated from the common-Pb-corrected $^{238}U/^{206}Pb$ (and $^{235}U/^{207}Pb$) ratio and measured $^{234}U/^{238}U$ ratio using in-house software. Uncertainties were estimated using a Monte Carlo approach. Initial ^{230}Th and ^{231}Pa are assumed to have been absent in the age/concordia calculations. Initial ^{234}U is determined based on the present-day $^{234}U/^{238}U$ ratio as part of the age calculation, much as in U-Th chronology.

Decay constants used are: ^{238}U: 1.55125×10^{-10}, ^{234}U: 2.82203×10^{-6}, ^{230}Th: 9.17055×10^{-6}, ^{226}Ra: 4.33488×10^{-4}, ^{235}U: 9.8485×10^{-10}, ^{231}Pa: 2.11583×10^{-5}, ^{232}Th: 4.9475×10^{-11} [18,37,38].

As a cross-check on this methodology, two layers of stalagmite SLL10-6, G and F, were also analyzed following the method of Mason et al. (2013)[34] involving chemical purification of Pb from subsamples to generate isochron ages. Within uncertainty, these agree with the analyses obtained with the simplified protocol outlined above. U-Pb ages were also cross-checked against U-Th ages determined for the parts of the samples <0.5 Ma old (Data Tables 1 and 2, ED 8).

Screening of data and data quality

Ledyanaya Lenskaya Cave

Of the 59 U-Pb analyses (Data Table 1) ^{238}U-^{234}U-^{206}Pb ages have been included from 52 analyses (ED 8A). Of the excluded analyses, one has no corresponding $^{234}U/^{238}U$ measurement (SLL10-4-B bottom), so an age cannot be calculated. Three analyses (two from SLL10-6-B and one from SLL10-6-B/C hiatus) are non-radiogenic and yield ages with unhelpfully large uncertainties, though usefully help to constrain the common Pb correction. Two analyses (SLL14-1-C centre and SLL9-1-A2) yield >1.5 Ma apparent ages, which are not reproduced in other analyses and appear inconsistent with the $^{234}U/^{238}U$ measurements; and one analysis (SLL10-4-A top) is both out of stratigraphic order and in disagreement with two other analyses from the same layer.

The remaining 52 ages are consistently in stratigraphic order. The c. 1.3-1.5 Ma age cluster is useful for demonstrating analytical robustness, since the common-Pb correction in these analyses is mostly small and layers can be dated in stratigraphic order with c. 40 ka age resolution, even without pre-concentration of Pb. The replication of ages of many growth periods between different samples, even where the magnitude of the common-Pb correction varies substantially, helps to validate the common-Pb value used to calculate the model ages and corroborates the analytical robustness of the method. The agreement of

the ages for SLL10-6-Ftop and SLL10-6-G with and without pre-concentration of U and Pb should also be noted (ED 8A).

^{235}U-^{207}Pb ages are also given for reference in Data Table 1 and are mostly concordant with the ^{238}U-^{234}U-^{206}Pb ages within error (ED 9) (or, in 5 cases, show only slight discordance). These small discordances can probably be attributed to uncertainties in the common Pb correction, and could be accounted for by shifts in the common Pb composition of a few percent.

Samples SLL10-4C, SLL10-5B, SLL10-9A, SLL10-9C and SLL14-1B bottom have notably low ^{235}U-^{207}Pb ages relative to their ^{238}U-^{234}U-^{206}Pb ages. None of these ^{238}U-^{234}U-^{206}Pb ages fails on the grounds of being inconsistent with stratigraphic position and they tend to replicate well in other samples (ED 8). It is likely that this discordance is an analytical artefact, specifically incomplete elimination of the molecular interference on ^{208}Pb. An extraneous contribution on ^{208}Pb will lead to overcorrection of the common Pb. Since the ^{207}Pb is typically some 20-30x more sensitive (Data Table 1) to the common Pb correction, a small overcorrection on the ^{206}Pb can correspond to a significant overcorrection on the ^{207}Pb, hence the ^{235}U-^{207}Pb ages appear anomalously young while the ^{238}U-^{234}U-^{206}Pb ages remain stratigraphically consistent.

The (near-)concordance of the majority of the ages provides confidence in the data from an analytical standpoint.

Botovskaya Cave <0.7Ma samples

Of the 13 analyses from Botovskaya Cave, 12 ^{238}U-^{234}U-^{206}Pb ages were calculated. The analysis that failed to produce an age was from unradiogenic calcite G layer in SB-01112, which is bracketed between more radiogenic aragonite layers, and so it still useful for constraining the common Pb composition. Ages fall between 0.4 and 0.7 Ma (Data Table 1), and are in stratigraphic order overlapping well with available U-Th ages (ED 8B). ^{235}U-^{207}Pb ages could only be calculated for four analyses and are of low precision, but they are all concordant with the ^{238}U-^{234}U-^{206}Pb ages (Data Table 1).

Botovskaya Cave pre- 0.7Ma samples

Botovskaya Cave shows an extensive 2 Ma and older record, which is the subject of ongoing investigation. Data of some of these samples are used to better constrain the common Pb correction in the present work (Data Table 1, ED 7), although the ages are not used here because no pre-0.7 Ma Botovskaya samples overlapping the older part of the Ledyanaya Lenskaya record have yet been identified.

U-Th chronology:

The U and Th analysis, as well as U-Th ages calculations were performed following Vaks et al (2013) SOM[14]. Twelve layers of five samples from Botovskaya Cave were dated. Dating results and their correction for initial Th were calculated using Isoplot 4.15[39] and are presented in Data Table 2. ^{238}U concentrations in calcite vary between 0.44 to 1.25 ppm, whereas in aragonite they vary from 40.4 to 136.7 ppm. ^{232}Th concentrations usually vary between 0.06 and 3.15 ppb. $^{230}Th/^{232}Th$ activity ratios in the analysed samples varied between 6322 to $>10^6$, and the $^{232}Th/^{238}U$ activity ratios varied between $4.78*10^{-4}$ and $8.94*10^{-7}$. Thus, correction for $Th_{initial}$ was negligible. Two ages from layer SB-01112-D were rejected because this layer is adjacent to a horizon with high porosity, representing a joint between a growth hiatus and a crack in the speleothem. The lower part of layer "SB-01112-D bottom" shows an age reversal, possibly due to U leaching. Other U-Th ages shown in ED 4, 5, 8 are taken from Vaks et al (2013)[14], slightly modified using updated half-lives of ^{234}U and ^{230}Th[18].

The ability of Arctic air to reach Ledyanaya Lenskaya Cave site

Arctic air masses bring polar air southward to substantially influence Siberian weather. In particular, these air masses are capable of bringing latent heat and moisture from still unfrozen Arctic Ocean into Siberian continental interior during the period of October-early November. During this time of the year the Arctic Ocean is still partly unfrozen and snow cover is forming over the Siberian landmass. To demonstrate that these incursions of Arctic air are capable of reaching the site of Ledyanaya Lenskaya Cave, we show on ED10 figure twelve examples of such snow events above Ledyanaya Lenskaya Cave. Three trajectories for air on elevations 500, 1500 and 5000m were calculated for each event with at least one trajectory in each

event starts in Arctic Ocean. These trajectories were assessed using the NOAA Hysplit program (https://ready.arl.noaa.gov/HYSPLIT.php)[40,41]. The proper timing of the weather events mentioned above was received from log data of Lensk meteorological station (number 24923), 139 km NW from Ledyanaya Lenskaya Cave (https://rp5.ru/Погода_в_Ленске,_Республика_Саха_(Якутия) (in Russian)[42]).

Methods References:

31 Tchebakova, N. M., Rehfeldt, G. E. & Parfenova, E. I. in *Permafrost Ecosystems. Ecological Studies (Analysis and Synthesis)* Vol. 209 (eds Osawa A. *et al.*) 427-446 (Springer, 2010).

32 Ford, D. & Williams, P. W. *Karst Geomorphology and Hydrology*. (Unwin Hyman, 1989).

33 Seligman, B. *The English language edition of the geocryological map of Russia and neighbouring republics. P.J. Williams and I.M.T. Warren. 1999. Ottawa: Collaborative Map Project. Handbook: 32 p, soft cover. ISBN 0-9685013-0-3. Map: 16 sheets (95 × 66 cm per sheet), scale 1:2,500,000. $US350.00*. 2009/10/27 edn, Vol. 36 (Cambridge University Press, 2000).

34 Mason, A. J., Henderson, G. M. & Vaks, A. An Acetic Acid-Based Extraction Protocol for the Recovery of U, Th and Pb from Calcium Carbonates for U-(Th)-Pb Geochronology. *Geostandards and Geoanalytical Research* **37**, 261-275, doi:10.1111/j.1751-908X.2013.00219.x (2013).

35 Hiess, J., Condon, D. J., McLean, N. & Noble, S. R. $^{238}U/^{235}U$ Systematics in Terrestrial Uranium-Bearing Minerals. *Science* **335**, 1610-1614, doi:10.1126/science.1215507 (2012).

36 Mason, A. J. & Henderson, G. M. Correction of multi-collector-ICP-MS instrumental biases in high-precision uranium-thorium chronology. *International Journal of Mass Spectrometry* **295**, 26-35 (2010).

37 Cheng, H., Edwards, R. L., Murrell, M. T. & Benjamin, T. M. Uranium-thorium-protactinium dating systematics. *Geochimica et Cosmochimica Acta* **62**, 3437-3452, doi:https://doi.org/10.1016/S0016-7037(98)00255-5 (1998).

38 Steiger, R. H. & Jäger, E. Subcommission on geochronology: Convention on the use of decay constants in geo- and cosmochronology. *Earth and Planetary Science Letters* **36**, 359-362, doi:https://doi.org/10.1016/0012-821X(77)90060-7 (1977).

39 Ludwig, K. A. in *Berkeley Geochronological Centre, Special Publication* Vol. 5 (ed Kenneth A. Ludwig) (Berkeley Geochronological Centre, Berkeley CA, USA, 2012).

40 Rolph, G., Stein, A. & Stunder, B. Real-time Environmental Applications and Display sYstem: READY. *Environmental Modelling & Software* **95**, 210-228, doi:https://doi.org/10.1016/j.envsoft.2017.06.025 (2017).

41 Stein, A. F. *et al.* NOAA's HYSPLIT Atmospheric Transport and Dispersion Modeling System. *Bulletin of the American Meteorological Society* **96**, 2059-2077, doi:10.1175/bams-d-14-00110.1 (2015).

42 Bulygina, O. N., Veselov, V. M., Razuvaev, V. N. & Aleksandrova, T. M. DESCRIPTION OF HOURLY DATA SET OF METEOROLOGICAL PARAMETERS OBTAINED AT RUSSIAN STATIONS, http://meteo.ru/english/climate/descrip12.htm, http://meteo.ru/english/climate/cl_data.php. (2014).

Corresponding author:

Anton Vaks, antonv@gsi.gov.il

Competing interests:

The authors declare no competing interests.

Data availability statement:

The chronology data from this article is available on NGDC database: Vaks, A. (2019): Speleothem chronology in Ledyanaya Lenskaya and Botovskaya caves used in publication "Paleoclimate evidence of vulnerable permafrost during times of low sea-ice" By Vaks, A. et al. 2019. British Geological Survey. (Dataset). https://dx.doi.org/10.5285/d56addfe-b7b8-4b70-9617-fadc1f7666b4

All data that support the findings of this study are available from the corresponding author on request as well.

Extended Data 1: Caves' maps. A) Map and cross-section of Ledyanaya Lenskaya Cave, with speleothem and temperature logger positions; B) Map of Botovskaya Cave with locations of speleothems and temperature loggers.

Extended Data 2: Temperature data inside and outside caves. A) Ledyanaya Lenskaya Cave air temperatures between March 2010 and December 2013; B) Comparison of air temperature in Ledyanaya Lenskaya Cave (from panel A), mean annual surface temperature and surface air temperature changes (Lensk meteorological station 24923 data); C) Monitoring of air temperatures inside Botovskaya Cave (February 2010 - February 2016); Between 2010 and 2014 temperatures were monitored deep inside the cave, whereas between 2015 and 2016 loggers were placed closer to the entrance; D) Comparison of Botovskaya Cave temperatures with mean surface temperature and surface temperature changes between February 2010 and July 2014 (data from temperature logger outside the cave).

Extended Data 3: Detailed permafrost maps. A) Permafrost map of the Ledyanaya Lenskaya Cave area[33], the cave site is marked by a magenta circle. Lensk and Olekminsk are marked by black circles. B) Permafrost map of the Botovskaya Cave area[33], the cave location is marked by magenta circle. Zhigalovo is marked by black circle. Types and thickness of the permafrost are shown below. In places with continuous permafrost (types 18-20), it covers >95% of the area, but may contain small unfrozen units (taliks), mainly under permanent bodies of water. Taliks may go through the entire permafrost layer (through taliks), or through part of it (not through taliks).

Extended Data 4: Pictures of speleothems' cross-sections with ages (in ka) from Ledyanaya Lenskaya Cave. Age uncertainties are 2σ. The U-Pb ages shown in black and a single U-Th age in stalactite SLL9-2[14] is shown in brown. Hiatuses are shown with red arrows. All speleothems are composed of calcite.

Extended Data 5: Pictures of speleothems' cross-sections with ages (in ka) from Botovskaya Cave. Age uncertainties are 2σ. The U-Pb ages shown in black and U-Th ages[14] are shown in brown. Most speleothems are composed of aragonite, except stalagmite SB-6919, and layers A-D, G in stalagmite SB-01112 which are calcitic.

Extended Data 6: Speleothems' petrography. A) Calcitic stalagmite SLL10-6 with its layered structure; B) Magnified area (5 to 3 mm - rectangle on the top of A) in crossed polar light, showing columnar crystals; C) Aragonitic stalagmite SB-7497(3) with fibrous crystals; D) Magnified area (3 to 1.5 cm) shown by black rectangle in C in plain polar light.

Extended Data 7: Common Pb composition assessment for Ledyanaya Lenskaya (upper) and Botovskaya (lower) caves. ^{234}U-^{206}Pb and ^{238}U-^{206}Pb appear on the left, and ^{235}U-^{207}Pb on the right, showing consistent common Pb values for each cave. The y-intercept represents the common lead ratio, yellow bars show the assigned range for common Pb in age calculations. Groups refer to the regression groups in Data Table 1 with solid black lines showing regression fits. Grey contours show the percentage change in calculated age resulting from changing the common Pb composition by its assigned uncertainty. Dashed black lines show reference isochrons and ungrouped data is shown by grey circles. Uncertainties (2σ) are sometimes smaller that the symbol size. Particular details for each plot:

A) Estimate of the common $^{208}Pb/^{206}Pb$ for Ledyanaya Lenskaya Cave in $^{234}U/^{206}Pb$- $^{208}Pb/^{206}Pb$ isotope space. ^{234}U is used in the plot instead of ^{238}U to suppress scatter in the $U/^{206}Pb$ ratio due to variations in the $^{234}U/^{238}U_{initial}$ ratio. All but two of the ungrouped data have age uncertainties due to common Pb of <1% and are thus insensitive to the common Pb correction. Most data that are more sensitive to the common Pb composition (i.e. those between the 1% and 3% contours) are included in the regressions to estimate the common Pb composition.

B) Equivalent plot in $^{235}U/^{207}Pb$-$^{208}Pb/^{207}Pb$ isotope space for the estimation of the common $^{208}Pb/^{207}Pb$ ratio for Ledyanaya Lenskaya cave. Group 3 and 4 correspond to the clump of ungrouped data close to the horizontal axis at c. 0.225 on plot A. Note that $^{235}U/^{207}Pb$ ages are substantially more sensitive to the common Pb correction; these ages are used as a check on U-Pb concordance rather than to derive the dates used in the paper.

C) Estimate of the common $^{208}Pb/^{206}Pb$ for Botovskaya Cave in $^{238}U/^{206}Pb$- $^{208}Pb/^{206}Pb$ isotope space. Groups 1, 3, 4 and 6 (plotted as squares) are unpublished data from c. 2 Ma samples included here only to provide additional constraint on the common Pb composition (Data Table 1). Ages used here are from the data plotted as circles. As for Ledyanaya Lenskaya Cave, the common Pb estimate includes the data for which the correction matters most as far as is possible.

D) Equivalent plot in $^{235}U/^{207}Pb$-$^{208}Pb/^{207}Pb$ isotope space for the estimation of the common $^{208}Pb/^{207}Pb$ ratio for Botovskaya Cave. $^{235}U/^{207}Pb$ data are more sensitive to the common Pb correction.

Extended Data 8: Detailed speleothems' chronologies. A) The chronology of Ledyanaya Lenskaya Cave speleothems with 95% confidence errors. Each column in the plot represents one individual speleothem named in bottom horizontal axis. In each column, the U-Pb ages (purple circles) appear in stratigraphic order from left (young) to right (old). For each U-Pb age the corresponding proportion of radiogenic ^{206}Pb (right vertical axis) is shown by red circles above. The U-Th age of the youngest layer A in the stalactite SLL9-2[14] is shown by blue circle (bottom-left). The two isochron ages of layers Ftop and G in SLL10-6 stalagmite are shown by olive circles. Several replicate age determinations for similar layers were performed and appear in the plot in the same order as shown in Data Table 1; B) Botovskaya Cave speleothems' U-Th ages (dark blue circles, left Y axis, Vaks et al, 2013[14] and current work) and U-Pb ages (light blue circles, left Y axis), the latter are given with percentages of radiogenic ^{206}Pb (red circles, right Y axis). All age uncertainties are shown by 95% confidence error bars. The stratigraphic age of the layers dated from stalagmite SB-01112 increases from left to right.

Extended Data 9: **^{238}U-^{234}U-^{206}Pb ages and concordance of ^{235}U-^{207}Pb ages for Ledyanaya Lenskaya Cave** (based on Data Table 1). Ages and age uncertainties are shown in black with the corresponding coloured error bar indicating the degree of concordance (^{235}U-^{207}Pb age as a percentage of the ^{238}U-^{234}U-^{206}Pb age; blue horizontal line indicates perfect concordance) of the ^{235}U-^{207}Pb age. Blue error bars indicate the analysis is concordant within error. Orange error bars denote slightly discordant analyses, where the apparent discordance is likely due to common Pb correction on ^{207}Pb. Red error bars denote analyses that are discordant with markedly low ^{235}U-^{207}Pb ages attributed to overcorrection of the common Pb due to a residual interference on ^{208}Pb. The numbers and bars in red show the percentage bias in the ^{238}U-^{234}U-^{206}Pb ages if the discordance of these samples is attributed to an interference on ^{208}Pb, based on the relative

sensitivity of the ^{235}U-^{207}Pb and ^{238}U-^{234}U-^{206}Pb ages to the common Pb correction (Data Table 1). Grey horizontal lines indicate where ages replicate in two or more speleothems. The biases in the ^{238}U-^{234}U-^{206}Pb ages attributed to the interference on ^{208}Pb do not change these ages outside of error, hence, the tendency of these ages to replicate well in other samples. The discordance arises almost entirely from the ^{235}U-^{207}Pb ages (which are not used), due to their vastly greater sensitivity to over-correction of the common Pb than the ^{238}U-^{234}U-^{206}Pb ages. Errors are 95% confidence. For each speleothem, the stratigraphic age of the dated layers increases from left to right.

Extended Data 10: HYSPLIT-model-based 7 day back-trajectories of 12 snow events in Ledyanaya Lenskaya Cave site. These snowfall events were accompanied by significant decrease in air temperature indicating that Arctic air was involved in the synoptic event. Six snow events occurred in October and first half of November 2012 (A – F), and other six events occurred in October and first half of November of 2013 (G – L). For each of 12 events, three back trajectories for elevations of 500, 1500 and 5000 m above sea level were calculated, with at least one of them originating in Arctic Ocean in each case. The dates and times of the events are as follows: A – 04/10/2012, 21:00; B – 07/10/2012, 21:00; C – 19/10/2012, 09:00; D – 21/10/2012, 15:00; E – 05/11/2012, 09:00; F – 11/11/2012, 09:00; G – 01/10/2013, 09:00; H – 09/10/2013, 00:00; I – 19/10/2013; 09:00; J – 25/10/2013, 09:00; K – 02/11/2013, 09:00; L – 10/11/2013, 09:00.

Identification information:

A – Job ID: 164576, Job Start: Tue 3 Sep, 12:19:42, UTC 2019; Meteorology: 0000Z, 1 Oct 2012 – GDAS1;

B – Job ID: 165119; Job Start: Tue 3 Sep, 12:46:49, UTC 2019; Meteorology: 0000Z, 1 Oct 2012 – GDAS1;

C – Job ID: 169518, Job Start: Sun 8 Sep 14:04:06, UTC 2019; Meteorology: 0000Z, 15 Oct 2012 – GDAS1;

D – Job ID: 169478, Job Start: Sun 8 Sep 13:58:40, UTC 2019; Meteorology: 0000Z, 22 Oct 2012 – GDAS1;

E – Job ID: 171083 , Job Start: Sun 8 Sep 15:42:40, UTC 2019; Meteorology: 0000Z, 1Nov 2012 – GDAS1;

F – Job ID: 171195, Job Start: Sun 8 Sep 15:47:51, UTC 2019; Meteorology: 0000Z, 8 Nov 2012 – GDAS1;

G – Job ID: 187728, Job Start: Fri 30 Aug 12:07:03 UTC 2019; Meteorology: 0000Z, 1 Oct 2013 – GDAS1;

H – Job ID: 172040, Job Start: Sun 8 Sep 16:46:37 UTC 2019; Meteorology: 0000Z, 8 Oct 2013 – GDAS1;

I – Job ID: 172169, Job Start: Sun 8 Sep 16:54:44 UTC 2019; Meteorology: 0000Z, 15 Oct 2013 – GDAS1;

J – Job ID: 172846, Job Start: Sun 8 Sep 17:16:55 UTC 2019; Meteorology: 0000Z, 22 Oct 2013 – GDAS1;

K – Job ID: 173152, Job Start: Sun 8 Sep 17:24:37 UTC 2019; Meteorology: 0000Z, 1 Nov 2013 – GDAS1;

L – Job ID: 173482, Job Start: Sun 8 Sep 17:32:06 UTC 2019; Meteorology: 0000Z, 8 Nov 2013 – GDAS1.

Parameters equal for all calculations in ED10:

Source: Lat. 60.371000, Long. 116.946472; Hights: 500 m, 1500 m, 5000 m AGL; Trajectory direction: Backward; Duration: 168 hrs; Vertical Motion Calculation Method: Model Vertical Velocity.

Figure 1:

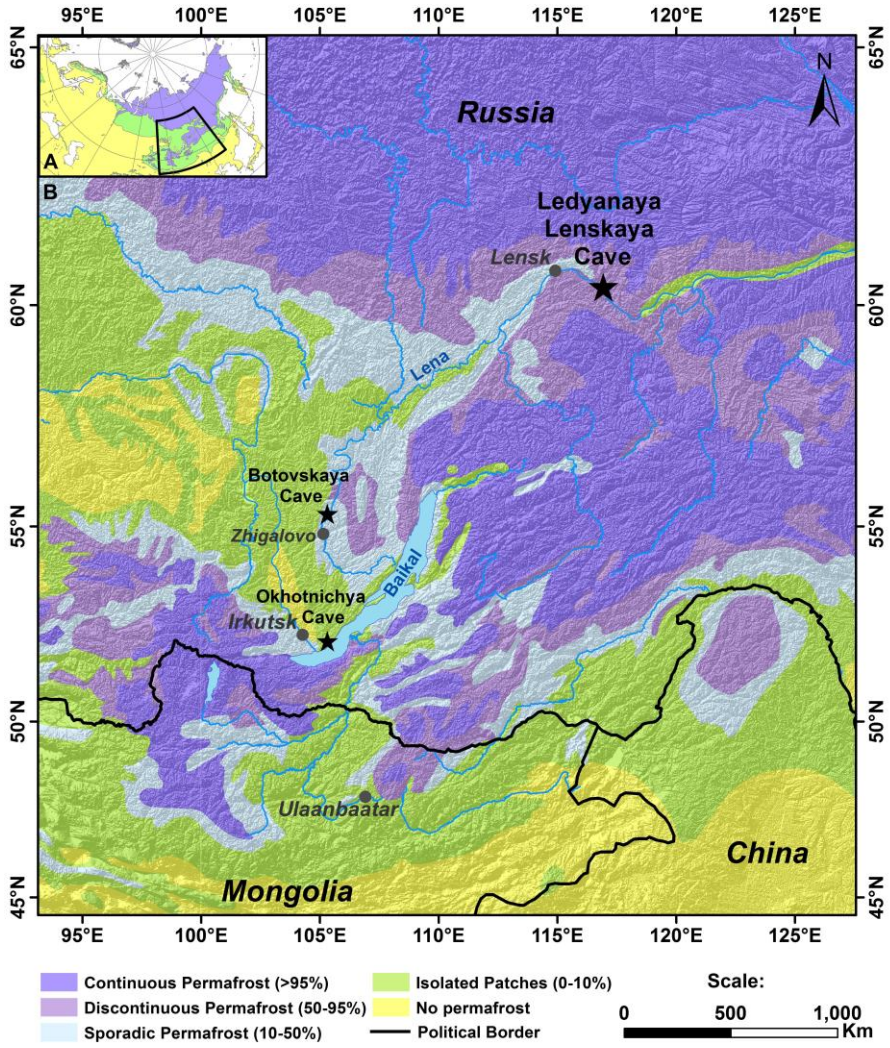

737 **Figure 2:**

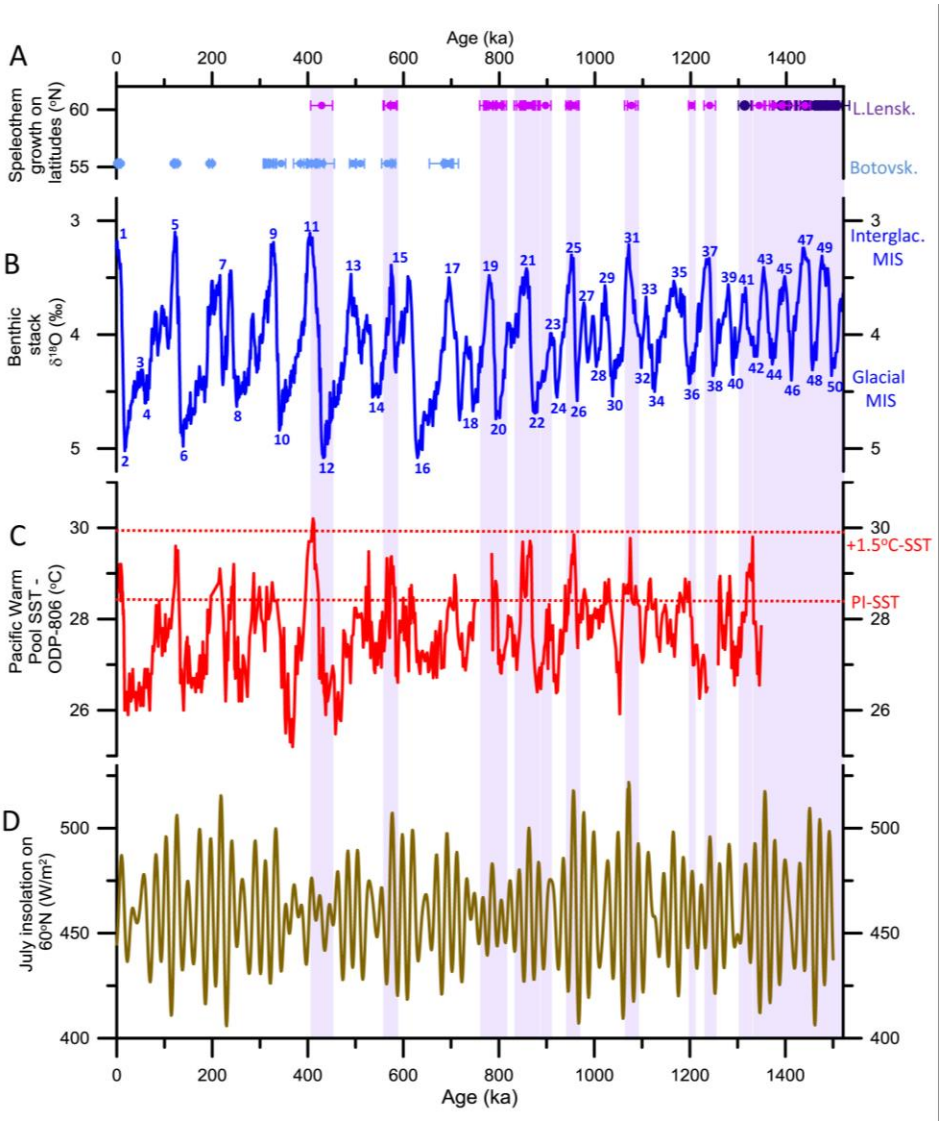

738

739

740

741 **Figure 3:**

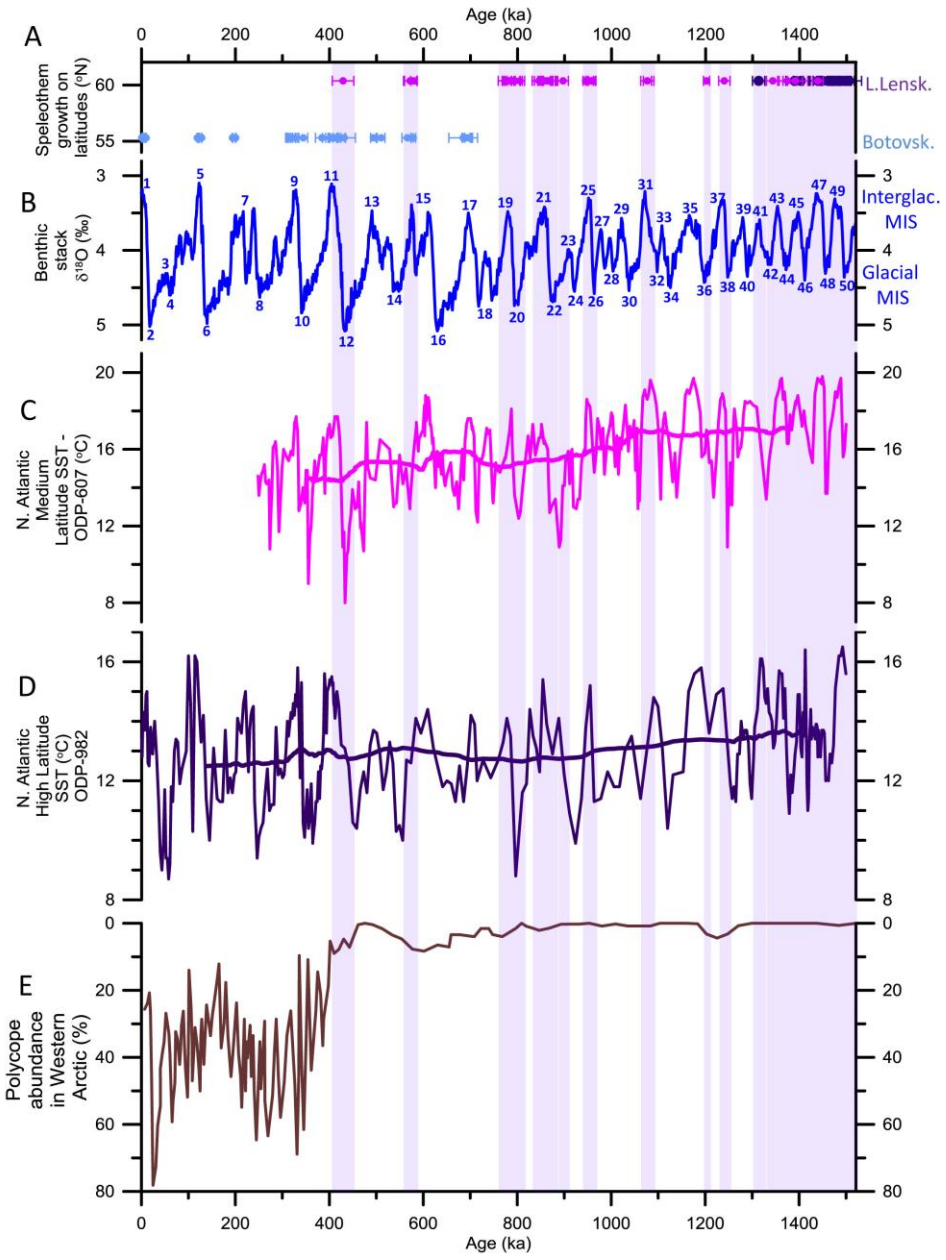

742